

# Enhancement of osteoblast activity on nanostructured NiTi/hydroxyapatite coatings on additive manufactured NiTi metal implants by nanosecond pulsed laser sintering

Biwei Deng<sup>1,2</sup>  
Angela Bruzzaniti<sup>3</sup>  
Gary J Cheng<sup>1,2</sup>

<sup>1</sup>School of Industrial Engineering, Purdue University, West Lafayette, IN 47907, USA; <sup>2</sup>Birck Nanotechnology Center, Purdue University, West Lafayette, IN 47907, USA;

<sup>3</sup>Department of Biomedical and Applied Sciences, Indiana University School of Dentistry, Indianapolis, IN 46202, USA

**Background:** The osteoinductive behaviors of nitinol (NiTi)-based metal implants for bone regeneration are largely dependent on their surface composition and topology. Continuous-mode laser sintering often results in complete melting of the materials and aggregation of particles, which lack control of heat transfer, as well as microstructural changes during sintering of the nanocomposite materials.

**Methods:** In the current study, in situ direct laser deposition was used to additively manufacture three-dimensional NiTi structures from Ni and Ti powders. The mechanical property of NiTi has been shown to be similar to bone. Nanosecond pulsed laser sintering process was then utilized to generate a nanoporous composite surface with NiTi alloy and hydroxyapatite (HA) by ultrafast laser heating and cooling of Ni, Ti, and HA nanoparticles mixtures precoated on the 3D NiTi substrates; HA was added in order to improve the biocompatibility of the alloy. We then studied the underlying mechanism in the formation of NiTi/HA nanocomposite, and the synergistic effect of the sintered HA component and the nanoporous topology of the composite coating. In addition, we examined the activity of bone-forming osteoblasts on the NiTi/HA surfaces. For this, osteoblast cell morphology and various biomarkers were examined to evaluate cellular activity and function.

**Results:** We found that the nanoscale porosity delivered by nanosecond pulsed laser sintering and the HA component positively contributed to osteoblast differentiation, as indicated by an increase in the expression of collagen and alkaline phosphatase, both of which are necessary for osteoblast mineralization. In addition, we observed topological complexities which appeared to boost the activity of osteoblasts, including an increase in actin cytoskeletal structures and adhesion structures.

**Conclusion:** These findings demonstrate that the pulsed laser sintering method is an effective tool to generate biocompatible coatings in complex alloy-composite material systems with desired composition and topology. Our findings also provide a better understanding of the osteoinductive behavior of the sintered nanocomposite coatings for use in orthopedic and bone regeneration applications.

**Keywords:** metal implants, bone regeneration, osteoinductive behavior, pulsed laser coating, biocompatibility, differentiation, alkaline phosphatase

Correspondence: Gary J Cheng  
School of Industrial Engineering, Purdue University, 610 Purdue Mall, West Lafayette, IN 47907, USA  
Email gcheng@purdue.edu

Angela Bruzzaniti  
Department of Biomedical and Applied Sciences, Indiana University School of Dentistry, DS243, 1121W Michigan Street, Indianapolis, IN 46202, USA  
Email abruzzan@iu.edu

## Introduction

Nitinol (NiTi) is considered to be a promising material for medical applications, due to its good resistance to corrosion and adequate biocompatibility, similar to Ti-6Al-4V and stainless steel.<sup>1</sup> In particular, NiTi has the closest elastic modulus to bone among common implant alloys, as well as the unique property of superelasticity and shape

memory effects. These properties open up the possibility for its use in medical devices that have tunable geometry, and the capability of applying a constant force, such as in internal fixation devices, scoliosis correction devices, and orthopedic implants.<sup>2-4</sup> Despite the wide usage of NiTi in biomedical applications, its biocompatibility is still controversial.<sup>5</sup> The potential concerns for NiTi include corrosion,<sup>6</sup> release of toxic Ni ions,<sup>7</sup> and surface-induced thrombus formation.<sup>8</sup> To overcome these negative effects, a biocompatible coating is needed, which can protect the surface of NiTi implant.

For metallic orthopedic applications, a well-known approach to boost bone regeneration on metallic implants is to form a composite coating with a bioceramic component on their surface. HA and Ca/P ceramic of other phases are materials of choice for the coating layer, since they are the main ceramic species in natural bone.<sup>9</sup> Many investigators have reported successful integration of HA coatings on various metallic substrates, such as Ti-6Al-4V,<sup>10-12</sup> stainless steel,<sup>13</sup> and NiTi,<sup>14</sup> resulting in positive effects on various aspects of bone regeneration. Recent studies took a step further to generate complex surface topology for HA or HA-containing coatings. It has been recognized that HA coatings with microstructural or nanostructural complexities have positive effects on osteoblast cell proliferation, differentiation and mineralization, as well as enhanced cell adhesion.<sup>15-18</sup> In addition to the topology effect, the nano-sized HA, which was the most common form of porous HA coatings, showed superior advantage compared with micron-grained HA, in terms of cell attachment and mineralization.<sup>19-21</sup>

There are many approaches for the deposition of HA coatings on top of a metallic surface, including plasma spray,<sup>19,22</sup> electrophoretic deposition,<sup>23</sup> pulsed laser deposition,<sup>24</sup> and biomimetic approaches.<sup>25</sup> Among these methods, plasma spray has been commonly applied in commercial biomedical HA coatings. However, plasma-sprayed HA coating is known to have problems of low crystallinity and poor interfacial bonding.<sup>26,27</sup> Other methods like biometric approaches, which emulate the natural bone mineralization process in ambient solution conditions, take several days to produce a high-quality HA coating.<sup>25</sup> In contrast, laser sintering of micro- or nano-sized particles is a manufacturing process that is easy to scale up. Importantly, laser sintering stands out with the advantages of homogeneous sintering of the composite layer, and strong adhesion of a coating layer with the substrate in designs such as gradient metal-HA coating.<sup>28-30</sup> Compared with the commonly used continuous-wave laser, the nanosecond pulsed laser has the ability to sinter metal powders with lower average

input power, while melting only the material surfaces due to the extra high cooling rate.<sup>31</sup> Thus, it has the potential to generate composite porous surfaces due to the limited flow time required for the melt metals.<sup>32</sup> To the best of the authors' knowledge, there is no one-step method to generate porous NiTi/HA coating directly from Ni, Ti, and HA powders. Furthermore, to understand and take advantage of the unique effects of nanosecond pulsed laser sintering (NPLS), it is crucial to study the underlying mechanism in the intermetallic alloy/ceramic system, which has remained elusive.<sup>33,34</sup> Moreover, though well regarded as a potential implant material,<sup>35</sup> laser-sintered NiTi/HA porous coating has not been well investigated for its biocompatibility related to osteoblast activities. In addition, the synergistic effect of the sintered HA component and the porous topology of the composite coating remain to be investigated.

In this study, NPLS was applied to generate a NiTi/HA composite coating layer on top of an additive manufactured NiTi substrate produced by direct laser deposition. The sintered NiTi/HA composite coatings exhibited submicron-scale porous surfaces. The NPLS process was studied regarding its effects on coating surface structures and sintered material microstructures. NiTi with these surface coatings were then used as substrates for osteoblast cell culture. The effectiveness of the composite coating towards cell proliferation and function was carefully evaluated through investigations of cell morphology and related biomarker expressions. The effect of HA and the pulsed laser-generated porous feature of the coating were, respectively, studied towards the final osteoinductive behavior.

## Materials and methods

### In situ direct laser deposition of NiTi substrates

We carried out the laser in situ synthesis of NiTi substrates using an Optomec LENS 750 system. The LENS system utilizes a continuous-wave, 500 W fiber laser to fuse powdered metals into fully dense or porous three-dimensional structures. The LENS system uses the geometric information contained in a Computer-Aided Design (CAD) solid model to automatically build up a component layer by layer. Additional software and closed-loop process controls ensure the geometric and mechanical integrity of the completed part. With the Optomec LENS system, the process is housed in a hermetic chamber, which is purged using argon so that the oxygen and moisture levels stay below 10 parts per million. The metal powder feedstock is delivered to the deposition head by two powder-feed systems. The NiTi substrate was directly laser-deposited from Ni and Ti powders, thus

eliminating the intermediate steps used to prepare pre-alloyed NiTi powders.

## Pre-coating of Ni/Ti/HA

Nano-sized titanium and nickel powder (30–50 nm dia.) were purchased from NanoAmor Inc. One hundred milligrams of Ni/Ti (1:1) powders were mixed with 0.1 g HA (Sigma-Aldrich, product #289396) and dispersed in 10 mL of 4% (wt%) polyvinylpyrrolidone (PVP) ethanol solution. The solution was put in strong sonication for 5 hours to ensure homogeneity. Then, the as-prepared viscous dispersion was drop-casted multiple times on NiTi alloy substrates, until desired thickness of coating layer was reached and dried out.

## NPLS processing

Pulsed neodymium-doped yttrium aluminum garnet (Nd:YAG) laser operating at 50 kHz and 1,064 nm wavelength was applied as the laser source. Pulse duration of the laser is 100 ns. A high-speed scanner (hurrySCAN II 14; SCANLAB GmbH, Puchheim, Germany) was aligned to direct and focus the laser beam onto a working surface in an air-tight chamber with quartz top. The chamber was connected to argon flow constantly to ensure the protective atmosphere while sintering. The applied laser power was 40 W. Rapid beam spot movement is realized by rotation of the galvo-motorized mirror inside the scanner, which has a resolution of 0.0008°. With a focus length of 200 mm, the X–Y resolution of the scanning pattern is 3 µm. Applied scan speed is 25 mm/s and laser pulse repetition rate is 20 kHz, so between each pulse, the movement of beam spot is 1.25 µm.

After NPLS process, the as-sintered samples were rinsed in ethanol followed by 5 minutes of sonication in ethanol. Post-acid etching, if needed, was done by immersing the sintered sample surface into dilute phosphoric acid (pH=3) for 5 minutes. According to the literature,<sup>36</sup> dilute phosphoric acid with pH <4.5 can effectively dissolve HA. We used lower pH to ensure that the HA can be removed completely within 5 minutes.

## Characterizations

Surface morphology was studied under field emission scanning electron microscopy (FESEM, Hitachi s-4800). X-ray diffraction spectrometry was performed on Bruker AXS D8 diffractometer with a scan speed of 8°/min. FEI Quanta 3D FEG dual-beam SEM with electron dispersive X-ray analysis capability was employed to obtain surface morphology as well as associated element information including spectra and mapping data. As for the fixing of cells on

ally plates, specimens were fixed in 2.5% glutaraldehyde in 0.1 M sodium cacodylate buffer, post-fixed in 1% osmium tetroxide, dehydrated in a graded ethanol series, transferred into hexamethyldisilazane, and air dried. Dried specimens were coated with platinum in a Cressington 208HR sputter coater to ensure the conductivity of the sample before SEM inspection.

Mechanical property tests were performed with a nanoindentation instrument (G200, Keysight). The elastic modulus  $E$  was measured with Berkovich indenter using the Oliver-Pharr method. The indentation depth is limited to 500 nm and the distance between two adjacent indentation locations is 4 µm. To test the crack resistance of the interface locations, we further performed indentations with cube corner indenter. A one-time indentation of 8.8 µm depth and a 5 × 5 indentation matrix of 4 µm depth were performed near the interface.

## Animal housing and preparation of osteoblast cell cultures

C57BL/6 mice were originally purchased from Jackson Laboratories and a breeding colony was established within the Indiana University School of Dentistry. A pair of male and female mice of 2–4 months of age were housed together for breeding. All experiments involving animals were approved by Institutional Animal Care and Use Committee (IACUC) of the American Association for Laboratory Animal Science and followed the NIH guidelines (Guide for the Care and Use of Laboratory Animals, 1996). Litters of pups were used as a source of neonatal calvaria, and male and female pups were pooled. Osteoblasts were prepared using the previously described protocol.<sup>37,38</sup> Briefly, calvaria from neonatal C57BL/6 mice 2–3 days old were pretreated with 10 mM EDTA in PBS for 30 minutes. Next, the calvaria were subjected to sequential collagenase digestions. Osteoblasts were collected following incubation in collagenase from fractions 3–5.<sup>37</sup> Osteoblasts were grown in alpha minimum essential medium (αMEM) with L-glutamine supplemented with 10% (v/v) FBS and 1% (v/v) P/S in an incubator at 37°C with 5% CO<sub>2</sub>, then expanded and passaged twice prior to use.

For experimentation, NiTi plates were cut by waterjet into 1 × 1 cm squares prior to cell culture experiments. Metals were sterilized by immersion in 70% ethanol and then air dried in a Biohazard Class II cell culture hood. Osteoblasts were trypsinized, seeded at 1 × 10<sup>5</sup> cells on NiTi metals, and then cultured in osteogenic media, which consists of αMEM plus 10% FBS and containing 10 µM ascorbic acid and 50 µM β-glycerol phosphate. Cells were cultured for up to 7 days in

osteogenic media to promote osteogenic differentiation and mineral deposition.<sup>39</sup>

Osteoblasts on metal plates were fixed with 4% formaldehyde in PBS for 15 minutes. Blocking was performed in 0.1% BSA + 0.05% saponin in PBS for 20 minutes, then labeled for actin with rhodamine phalloidin (Invitrogen, R415) collagen (Chemicon, MAB1330). Nuclei were stained with 300 nM DAPI (Invitrogen D1306), which is a fluorescent stain that binds strongly to A–T-rich regions in DNA. Antibodies were diluted 1:100 in blocking solution and incubated with cells overnight. The secondary antibody used for collagen was goat anti-mouse IgG Dylight 488 Conjugated (35502) and was used at 1:100 dilution for 1 hour. After labeling, cells were washed in PBS for 5 minutes × 3 times, followed by mounting with Invitrogen Prolong Gold antifade (P36934). Cells were imaged using a Leica DMI4000B inverted microscope with attached Retiga digital camera, and using Image Pro software (Media Cybernetics, Inc., Bethesda, MD, USA).<sup>39</sup>

## Quantitative real-time PCR (qPCR)

qPCR was performed as previously described.<sup>39</sup> Briefly, total RNA was isolated from samples using RNAeasy kit (Qiagen). DNase I (Thermo-Fisher)-treated RNA was used to generate cDNA by reverse transcription according to the manufacturer's instructions (First Strand cDNA Synthesis Kit; Roche Applied Science). qPCR reactions were performed in a BioRad CFX detection system using SYBR green PCR reagents as described by the manufacturer. A calibration curve was performed for each primer pair, and all oligonucleotides were tested to ensure specificity and sensitivity. Ribosomal RNA (18S) was used as an endogenous control. The expression levels of the target genes in each sample were calculated by normalizing the mRNA level of a particular gene against 18S ribosomal RNA, which is considered a stable housekeeping gene. The following oligonucleotide primer pairs were used:

18S	Forward: 5' AGTCCCTGCCCTTTG TACACA Reverse: 5' CGATCCGAGGGCC TCACTA
Alkaline phosphatase (ALP)	Forward: 5' ACTGATGTGGAATAC GAACTGGATGAGAAGG Reverse: 5' CAGTCAGGTTGTTCC GATTCAATTCATACTGC
Collagen type I	Forward: 5' AACCTGGTGC GAA AGGTGAA Reverse: 5' AGGAGCACCAACGTT ACCAA

Osteocalcin (OCN)	Forward: 5' TCTCTCTGACCTC ACAGATGCCAAGC Reverse: 5' GGACTGAGGCTCCAA GGTAGCG
β-Actin	Forward: 5' TCACCCACACTGTG CCCATCTACGA Reverse: 5' CAGCGGAACCGCTC ATTGCCAATGG.

## Results and discussion

### Porous surface microstructure

The direct laser deposition method which additively manufactures the NiTi substrates is depicted in Figure 1A. The laser beam heats up the projected metal powders at the desired location and in situ synthesizes NiTi to build the required three-dimensional structure. As an example, Figure 1B and C shows a tensile test sample and a hip implant fabricated from in situ direct laser deposition, respectively. The quality of NiTi processed by in situ direct laser deposition, including the microstructure and phase compositions, has been verified in previous reports.<sup>40,41</sup>

Following the direct laser deposition of NiTi substrates, NPLS is used to generate porous NiTi/HA composite coatings. To verify the generation of the complex surface structures, we prepared coatings of either sintered NiTi (sNiTi), sintered NiTi/HA (sNiTi/HA), or sintered NiTi/HA with posttreatment of phosphoric acid (sNiTi/HA-acid), on top of NiTi alloy plates, as illustrated in Figure 1D and E.

The generation of pores during NiTi alloy sintering has been previously reported.<sup>42</sup> Factors that could contribute to the pore formation are gap between powders, volatilization of impurities, Kirkendall effect due to different atom diffusion rate, and volume shrinkage during NiTi alloying. Apart from the intrinsic pore generation mechanisms in the alloy system, HA also plays a role in formation of porosity. An increased porosity along with balling effect was reported in the laser sintering powder system with the presence of second-phase particles due to the Marangoni effect.<sup>43</sup> This means that the HA particles, as a secondary phase in the NiTi/HA system, can affect the surface morphology because of differences in surface energies. Moreover, laser sintering involves a more rapid heating/cooling process than, for example, isothermal heating in a furnace. Figure 1F demonstrates the proposed pore formation corresponding to the presence of HA nanoparticles. The increased surface energy in the coating provides the initiatives for pores to form. The pores generated are less likely to dissipate during the melting process due to insufficient action time.<sup>44</sup>



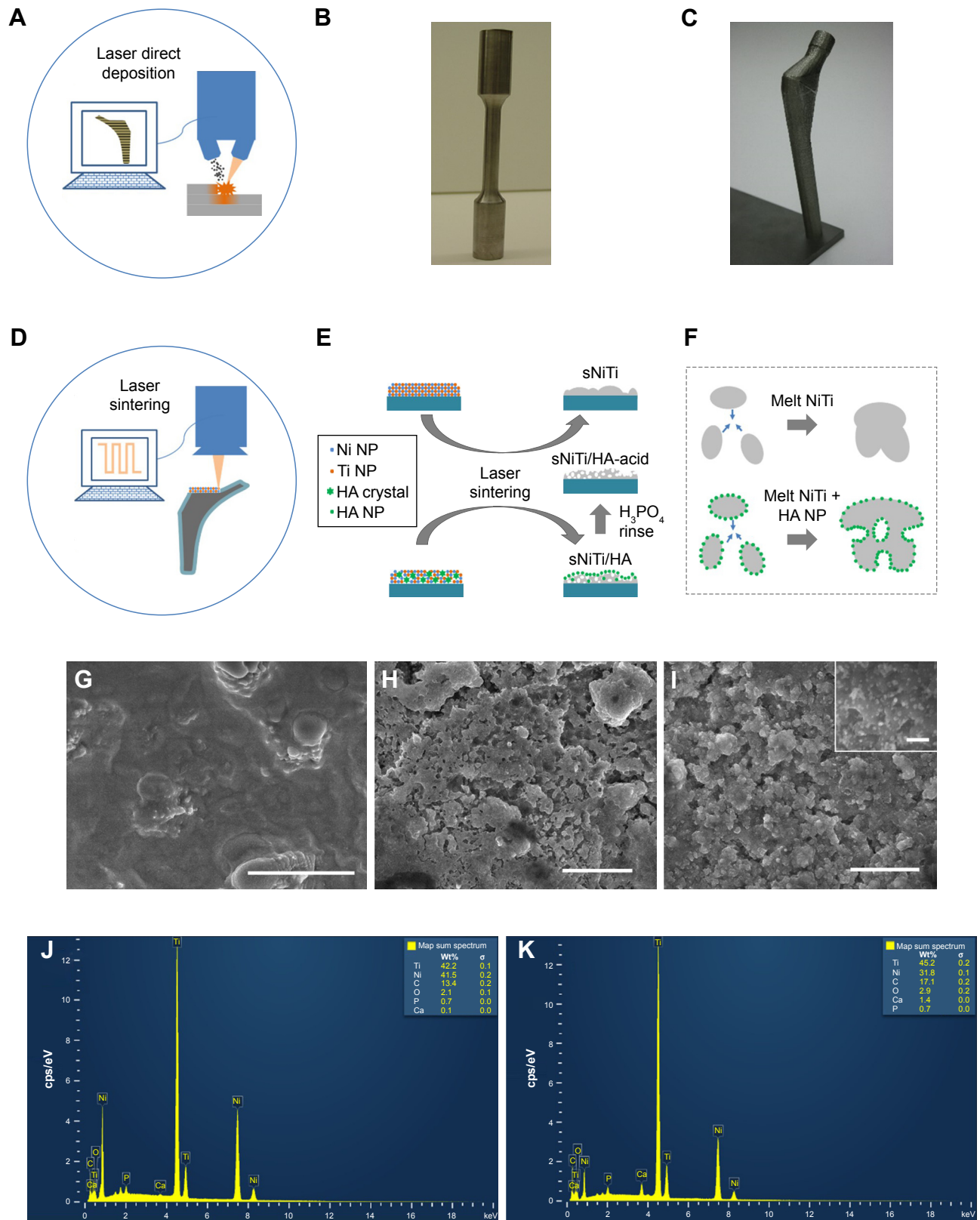


**Figure 1** (A) Schematic figure depicting the additive laser direct deposition of arbitrary 3D parts (B) Photos of a tensile test sample and a hip implant produced by additive laser direct deposition of NiTi (C) Surface of NiTi by additive laser direct deposition observed under scanning electron microscope, showing dense microstructure. Scale bar: 50  $\mu$ m (D) Schematic figure for NPLS of composite nanocoatings on arbitrary 3D parts (E) Preparation process of sNiTi, sNiTi/HA-acid, and sNiTi/HA. These three types of samples were used as cell test substrates. (F) Proposed pore formation mechanism during NPLS assisted by HA nanoparticles; (G) Surface structure of sNiTi; (H) Surface structure of sNiTi/HA-acid; (I) Surface structure of sNiTi/HA, with high-magnification image insert; (J) EDS spectrum from sNiTi/HA-acid; (K) EDS spectrum from sNiTi/HA. Scale bar: 5  $\mu$ m for (G–I) and 200 nm for insert (G).

**Abbreviations:** HA, hydroxyapatite; NiTi, nitinol; NPLS, nanosecond pulsed laser sintering; sNiTi, sintered NiTi.

The top surfaces of sNiTi, sNiTi/HA-acid, and sNiTi/HA metals are shown in Figure 1G–I. While the surface of sNiTi was overall smooth, the surface of sNiTi/HA-acid and sNiTi/HA featured micron and submicron-sized pore structures. The different surface structures observed can be explained by the effect of HA on pore generation as described above. On the surface of sNiTi/HA, the HA nanoparticles with the size of 10–20 nm were embedded throughout. Noting that the raw material of HA did not come in the form of nanoparticles, it is likely that the HA powders were melted or ablated into a nanoparticle form during the NPLS process. On the other hand, for the sNiTi/HA-acid surface, the HA nanoparticles were deliberately etched out by treatment with dilute phosphoric acid. It is worth noting that the nano-sized HA particles were rapidly etched out by dilute phosphoric acid, while the alloy matrix could resist the short-time etching, retaining the micron-scale pores on the surface. As discussed below, the sNiTi/HA-acid samples were used as a control group to show the effects of a porous structure on osteoblast activity.

Next, we used EDS analysis to confirm the element composition of the sNiTi/HA and sNiTi/HA-acid surfaces. The EDS signals were collected on specific areas of each substrate, as in Figure 1J and K, and the signals from elements Ni, Ti, Ca, P, O, and C were identified and listed in Table 1. Compared with the initial weight ratio of Ni, Ti, and HA (1:1:1), the element approximation of Ca and P on the sNiTi/HA sample was low. A possible reason for this could be that laser ablation caused mass losses of the coated HA during the initial sintering process. In addition, the carbon content may come from the incomplete vaporization and carbonization of the polyvinylpyrrolidone (PVP) binder. The diminished Ca signal in the EDS spectrum of sNiTi/HA-acid compared with sNiTi/HA provided confirmation that the HA was etched out of the coating by treatment with dilute phosphoric acid.

## Structural and mechanical analysis

To investigate the composition of the sintered coating, we analyzed X-ray diffraction spectra of the NiTi substrate, the pre-coated layer, and the sintered coating, as shown in Figure 2A and B. The pre-coating layer consists of nickel,

titanium, and HA, each showing its distinct XRD peaks. The NiTi peak from the substrate plate also appeared in the spectrum. According to the nickel-titanium phase diagram, NiTi is not the eutectic phase with lowest melting point. During the heating process of sintering, Ni and Ti were sintered and together formed NiTi; however, during the cooling process, phases like  $Ti_2Ni$  and  $Ni_4Ti_3$  might be generated.<sup>34</sup> It has previously been reported that laser melting causes multiple phase generation in NiTi alloy, which could support the mechanism above. In the X-ray diffraction spectrum of the pulse laser-sintered NiTi/HA coating, the only intermetallic alloy phase detected was NiTi, in which B2 is the primary phase with presence of the B19 phase. Note that the original Ni and Ti metal signals were no longer present, indicating that the two distinct metal nanoparticles were consumed entirely in alloying of NiTi, even though minimal amount of the Ti element in form of TiC was present as impurities. Suppression of  $Ni_4Ti_3$  and  $Ti_2Ni$  generation can be attributed to the fast melt/solidify process of the NPLS. After melting, the Ni and Ti nanoparticles can fuse within a short period of time into a homogeneous alloy, due to their ultra-small size. When the molten alloy solidifies, the fast cooling process does not allow enough time for NiTi to separate into other phases by recrystallization or aging,<sup>45</sup> resulting in NiTi as the final phase.

In addition to NiTi alloying, the microstructure of HA also evolves during NPLS. In Figure 2B, the signals from crystalline HA become relatively weak after the sintering process. This phenomenon was also reported by other researchers using laser sintering HA composite.<sup>28</sup> Depending on the quality of HA, annealing at temperatures as low as 600°C could cause HA to transform into  $\beta$ -tricalcium phosphate (TCP),<sup>46,47</sup> which will cause a reduction in the HA signals. However, in our case, the  $\beta$ -TCP phase was not detected. In the NPLS process, the peak temperature of a heated area could exceed the melting temperature of HA (around 1,100°C), which would likely cause HA to melt and transform to an amorphous state. Subsequently, the transformation from amorphous HA to crystalline HA or  $\beta$ -TCP during the solidification process could be suppressed by the fast cooling rate. In support of this, other amorphous HA generation methods suggest a similar mechanism with low substrate temperatures, for example, pulsed laser deposition (PLD) and plasma spraying.<sup>24,48</sup>

To study the mechanical property of the NPLS processed composite coating, and its adhesion to the NiTi substrate, nanoindentation tests were conducted on the cross section of the sintered plate. Figure 2C demonstrates a clear difference in the modulus and hardness between the NPLS processed

**Table 1** Weight ratios of various elements on sNiTi/HA and sNiTi/HA-acid samples from quantitative EDS analysis

Element wt%	Ti	Ni	C	Ca	P
sNiTi/HA	46.2	31.8	17.1	1.4	0.7
sNiTi/HA-acid	42.2	41.5	13.4	0.1	0.7

**Abbreviations:** HA, hydroxyapatite; NiTi, nitinol; sNiTi, sintered NiTi.

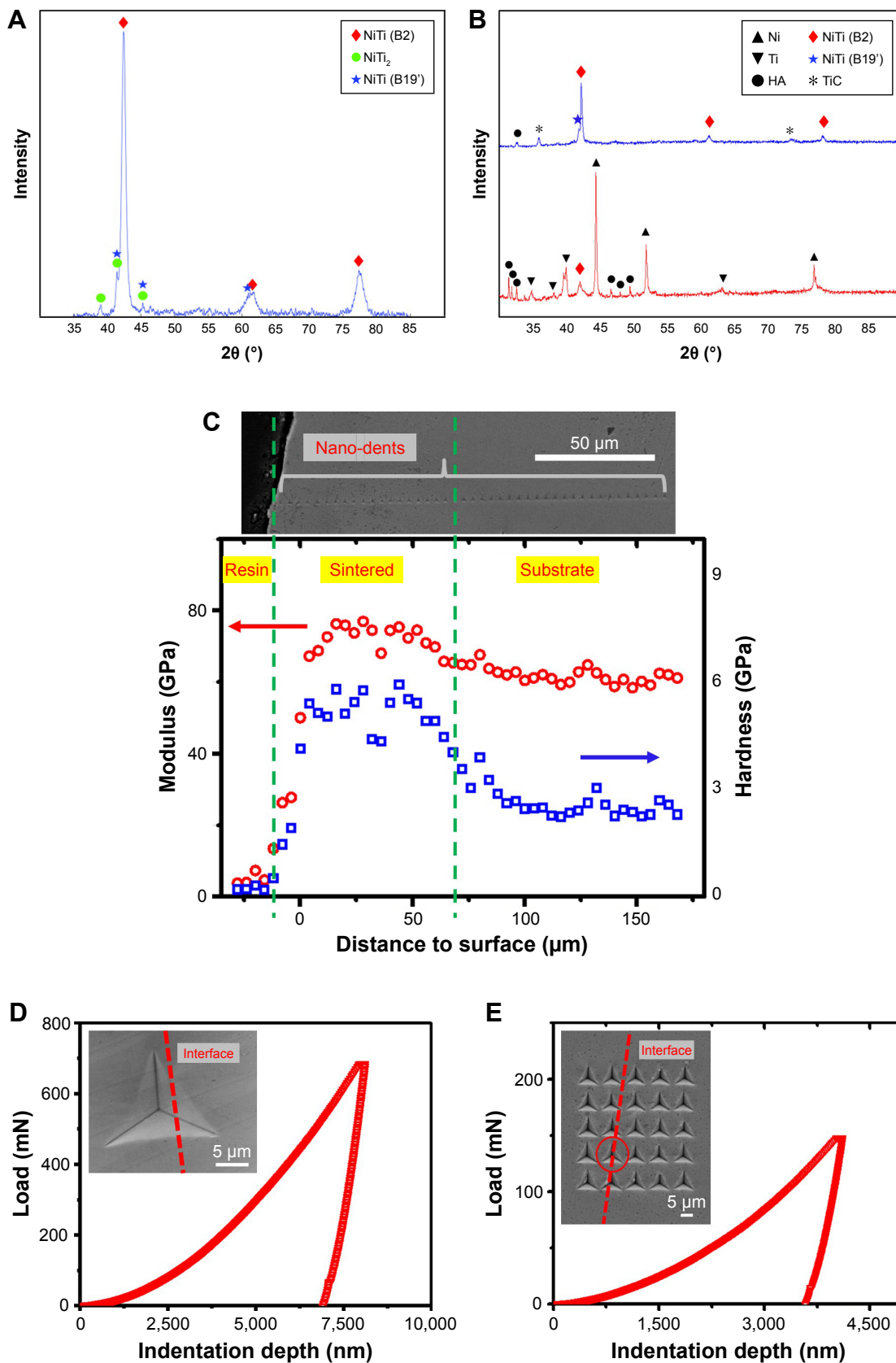


**Figure 2** (A) XRD analysis of the nitinol sample synthesized by laser direct deposition; (B) XRD pattern of pre-coated layer (red) and nanosecond pulsed laser-sintered coating of NiTi/HA (blue); (C) Nanoindentation test showing modulus and hardness along the sample depth; the sNiTi/HA coating shows higher modulus and hardness than the NiTi substrate; (D) and (E) Load-displacement relations from nanoindentation test with cube corner indenter near the interface between the coating and the substrate; inserted are the SEM observation of the corresponding dents.

**Abbreviations:** HA, hydroxyapatite; NiTi, nitinol; sNiTi, sintered NiTi.

NiTi/HA layer and the NiTi substrate. Due to good sintering effects, the boundary between the NiTi/HA layer and the NiTi substrate is hardly identifiable in the SEM image of the polished cross section. However, from the modulus-distance data, we determined that the coating thickness was around 80  $\mu\text{m}$ . For the sintered NiTi/HA layer, the modulus and hardness were  $71.1 \pm 4.2$  and  $4.2 \pm 0.8$  GPa, respectively, while for the NiTi substrate, the modulus and hardness were  $61.4 \pm 1.7$  and  $1.7 \pm 0.3$  GPa, respectively. The reason for the coating having a higher modulus/hardness value may be due to the addition of the HA nanoparticles to the matrix, or the thermal effect caused by the rapid laser heating/cooling.

To evaluate the attachment between the coating and substrate, we used a cube corner indenter to probe the cross-sectional interface. Figure 2D and E shows the load-displacement relations from nanoindentation test with cube corner indenter right above (Figure 2D) and across the interface (Figure 2E) between the coating and the substrate. As shown in Figure 2E, a one-time indentation of 8.8  $\mu\text{m}$  depth and a  $5 \times 5$  indentation matrix of 4  $\mu\text{m}$  depth was performed. No cracks or delaminations were observed in the corresponding SEM images. In addition, no fracture feature (pop-in or ductile failure) in the load-indentation depth curves was observed. These results suggested that the interface between the coating and substrate was resistant to crack initiations.

## Osteoblast culture

Osteoblasts are the primary bone-forming cells in the body. As osteoblasts mature, they secrete collagen, which becomes mineralized with  $\text{Ca}^{2+}$  and  $\text{PO}_4^{3-}$  deposits. To determine whether the introduction of HA, and the pore structures present on sNiTi/HA and sNiTi/HA-acid plates, affected their cellular biocompatibility, we plated primary murine osteoblasts on either sNiTi, sNiTi/HA, or sNiTi/HA-acid plates. Osteoblasts plated on each substrate/plate were cultured for 3 days in osteogenic media to promote their differentiation into mature cells that are capable of mineral deposition. After fixation and gold sputtering, the cell monolayer was imaged by SEM.

As shown in Figure 3A–C, osteoblasts formed a monolayer on top of the sNiTi, sNiTi/HA, and sNiTi/HA-acid plates. The red arrows in Figure 3B and C highlight the lamellipodial cell extensions of osteoblasts on the sNiTi/HA and sNiTi/HA-acid plates, while in Figure 3A, there was no sign of lamellipodial extensions. Mineral deposits (highlighted by yellow arrows) of different densities were also observed across the three samples: sNiTi/HA > sNiTi/HA-acid > sNiTi. Moreover, osteoblasts assumed a more

three-dimensional domed shape in sNiTi/HA and sNiTi/HA-acid plates compared with the flattened cells observed on the sNiTi plates, as shown in Figure 3D and E. In addition, mineral deposits on the extracellular matrix were evident. Next, the osteoblast monolayers were imaged in cross section to better examine fibrous structures (highlighted in yellow in Figure 3F–H). Compared with the fibrous structures within the osteoblast monolayer in the control sNiTi plates shown in Figure 3F, we observed an increase in osteoblast-associated fibrous structures associated with the sNiTi/HA and sNiTi/HA-acid (Figure 3G and H, respectively). We also observed a few microspheres attached to the bottom of cell monolayer as shown in Figure 3H (see red rectangles). These fibrous structures and microspheres most likely represented increased formation of a collagen-containing extracellular matrix. Together, these data provided support that the sNiTi/HA and sNiTi/HA-acid coatings, and in particular the presence of HA, promoted the differentiation of osteoblasts, resulting in an increase in extracellular matrix generation and mineral deposition.

After osteoblasts were imaged by SEM, the cell monolayer was removed by peeling, and the subcellular morphology of each plate surface was imaged as shown in Figure 4A, C and E. On the sNiTi plate (Figure 4A), the surface features were similar to plates that had not been cultured with osteoblasts. However, on both the sNiTi/HA-acid and sNiTi/HA samples, the metal plate surfaces were found to be covered in part with nano-sized particles (indicated in Figure 4C and E, by the red dashed line). We also observed that the area covered by the nano-sized particles was denser on the sNiTi/HA plate than the sNiTi/HA-acid plate. To further confirm and analyze the content of the subcellular layer generated by osteoblasts, EDS element mapping analysis was performed on representative areas of the sNiTi, sNiTi/HA-acid, and sNiTi/HA plates. As expected, the subcellular structure of the control sNiTi plate displayed a relatively uniform carbon element distribution, as shown in Figure 4B. As described in Table 1, the carbon content due to PVP carbonization on the sNiTi/HA and sNiTi/HA-acid plates before cell culture was 13.4% and 17.1%, respectively. As shown in Table 2, the carbon element weight ratio on sNiTi after osteoblast culture was 11.6%, which was around the same level as the carbon content levels from PVP carbonization. In contrast, after culture with osteoblasts, the subcellular structure showed a significantly higher carbon content of 44.4% for sNiTi/HA-acid and 67.7% for sNiTi/HA, compared with the 11.6% on sNiTi plates. The carbon element mapping areas in Figure 4D and F were similar to those observed in Figure 4C and E, indicating that the increased carbon



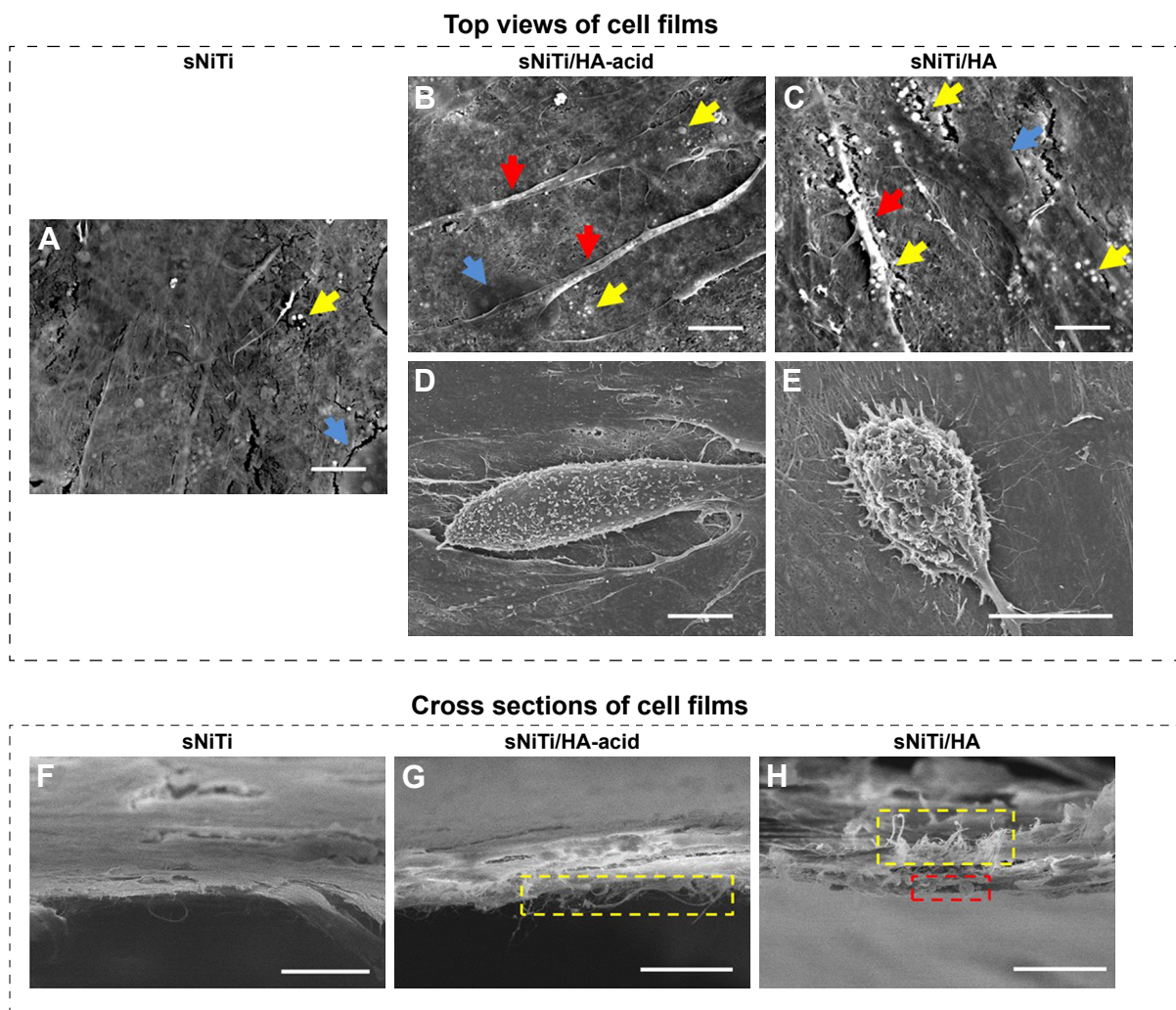


**Figure 3** Osteoblast morphology on different sNiTi plates.

**Notes:** After 3 days of osteoblast culture, the top view of the cell monolayers was imaged by SEM: (A) sNiTi; (B) and (D) sNiTi/HA-acid; (C) and (E) sNiTi/HA. Representative areas in (A–C) showing mineral deposits (yellow arrows), cell nuclei (blue arrows), and lamellipodia (red arrows). Some cells displayed a dome shape on sNiTi/HA-acid, as in (D); and sNiTi/HA, as in (E); no similar cells were found for sNiTi. Cross sections of the osteoblast monolayer were also imaged: (F) sNiTi; (G) sNiTi/HA-acid; (H) sNiTi/HA. A fibrous structure which is highlighted by yellow rectangles was observed in (G) and (H) and possibly represents extracellular matrix. The red rectangle in (H) indicates possible mineralized microspheres attached to the cell monolayer. Scale bar: 10  $\mu\text{m}$ .

**Abbreviations:** HA, hydroxyapatite; NiTi, nitinol; sNiTi, sintered NiTi.

content was attributed to plate areas previously covered by osteoblasts. In addition, Ca and P levels were not high within highlighted areas on the sNiTi/HA or sNiTi/HA-acid plates, suggesting that the carbon-rich layer does not contain a heavily mineralized component. These findings suggest that the carbon-rich layer may be due to higher levels of collagen or protein production by osteoblast on the sNiTi/HA-acid and sNiTi/HA plates, compared with sNiTi plates. Notably, fractured lamellipodial extensions and attached cells were found on the dense carbon-rich layer on sNiTi/HA, shown in Figure 4G (red arrows). It is also possible that enhanced cell attachment on the sNiTi/HA resulted in incomplete removal of osteoblasts from the HA-coated plated.

To further confirm the differentiation and activity of osteoblasts on the different sNiTi plate surfaces, pre-osteoblasts

were plated directly on the plates and cultured for 3 days in osteogenic media to promote their differentiation into mature osteoblasts capable of secreting collagen and mineralizing the extracellular matrix. Each step of the osteogenesis process is well characterized by the expression of specific protein and mRNA markers, including ALP, OCN, collagen, and others. Therefore, after culture on the metals, the cells were then lysed and quantitative real-time PCR was performed to examine changes in mRNA expression of several osteoblast genes. Specifically, we examined the expression of 1) collagen type 1, which is produced early in the osteoblast differentiation process and is a major structural component of the extracellular matrix which is later mineralized to form bone; 2) ALP, which is an enzyme expressed in the membrane of active osteoblasts and is essential for their ability to

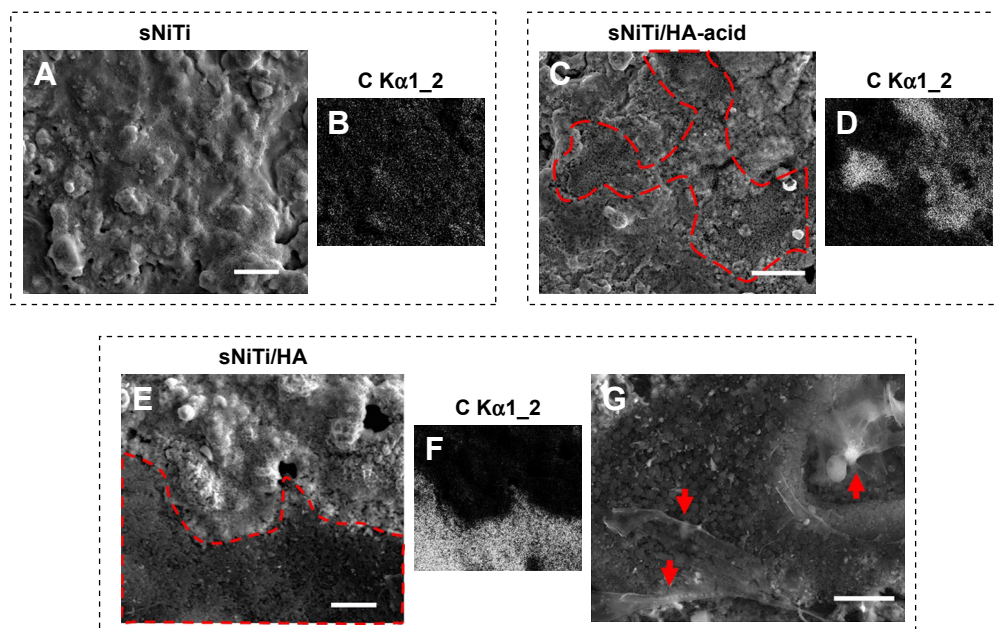


**Figure 4** Subcellular morphology of plates after osteoblast culture.

**Notes:** (A) sNiTi; (C) sNiTi/HA-acid; and (E) sNiTi/HA plates after osteoblasts were cultured for 3 days. In (C) and (E), the red dashed lines indicate the borders between the carbon-rich layers identified by carbon element mapping, which was generated by osteoblasts, compared with bare areas. (B, D and F) are representative images showing the carbon element mapping for imaged areas on sNiTi, sNiTi/HA-acid, and sNiTi/HA, respectively. (G) Magnified morphology of the highlighted area in (E) showing fractured lamellipodial cell extensions and cells (red arrows). Scale bar: 10  $\mu$ m.

**Abbreviations:** HA, hydroxyapatite; NiTi, nitinol; sNiTi, sintered NiTi.

mineralize the extracellular matrix;<sup>49</sup> and 3) OCN, which is a non-collagenous protein that is expressed during late stages of the osteoblast differentiation process and is required for mineralization and calcium homeostasis in vivo.

As shown in Figure 5, collagen mRNA expression was increased by 19% for sNiTi/HA-acid plates, and 203% for sNiTi/HA, compared with osteoblasts grown on the sNiTi substrate. These findings are consistent with the increased carbon element mapping on the sNiTi/HA-acid and sNiTi/HA plates. Note that the sNiTi/HA-acid sample represents a porous coating without HA content. From this, it can be inferred that the presence of intact HA coating, combined with a complex topology, led to a significant increase in collagen expression, compared with the sNiTi plates. As shown in Figure 5B, ALP expression was increased 237% and 386% for osteoblasts grown on the sNiTi/HA-acid and sNiTi/HA plates, respectively, compared with the control

**Table 2** Weight ratios of elements on subcellular structures after culture with osteoblasts for 3 days. sNiTi and highlighted areas in Figure 4 for the sNiTi/HA and sNiTi/HA-acid samples were analyzed using quantitative EDS analysis

Element wt%	Ti	Ni	C	Ca	P
sNiTi	48.9	39.0	11.6	NA	0.5
sNiTi/HA-acid	32.3	22.8	44.4	0.3	1.5
sNiTi/HA	18.1	16.2	67.7	0.5	1.2

**Abbreviations:** HA, hydroxyapatite; NiTi, nitinol; sNiTi, sintered NiTi.

sNiTi plates, suggesting that the structured coating and the presence of HA stimulated osteoblast maturation and mineralizing activity. We also found that OCN was higher in osteoblasts cultured on sNiTi/HA-acid and sNiTi/HA plates, compared with sNiTi (Figure 5C). Unexpectedly, OCN, which is a late marker of osteoblast activity, was higher in osteoblasts grown on the sNiTi/HA-acid surface, compared with sNiTi/HA. The reason for this finding may be due to the presence of additional nanovoids generated on the sNiTi/HA-acid surfaces following acid etching which may have led to more accelerated differentiation and mineralization, compared with the intact sNiTi/HA surfaces. In support of this, others have also reported that the increased roughness of metal surfaces after acid etching influences OCN levels and osteoblast maturation.<sup>50</sup> Nevertheless, both the sNiTi/HA and sNiTi/HA-acid surfaces demonstrate an overall higher level of osteoblast activity compared with the control sNiTi plates. Together, these data demonstrate that the sNiTi/HA and sNiTi/HA-acid surfaces were osteoinductive.

Osteoblast adhesion to the extracellular matrix involves the formation of integrin-associated focal adhesion complexes.<sup>51,52</sup> In agreement with an increase in focal adhesions in osteoblasts, the expression of the focal adhesion kinase (FAK) was increased by 35% when osteoblasts were grown on sNiTi/HA, compared with sNiTi or sNiTi/HA-acid

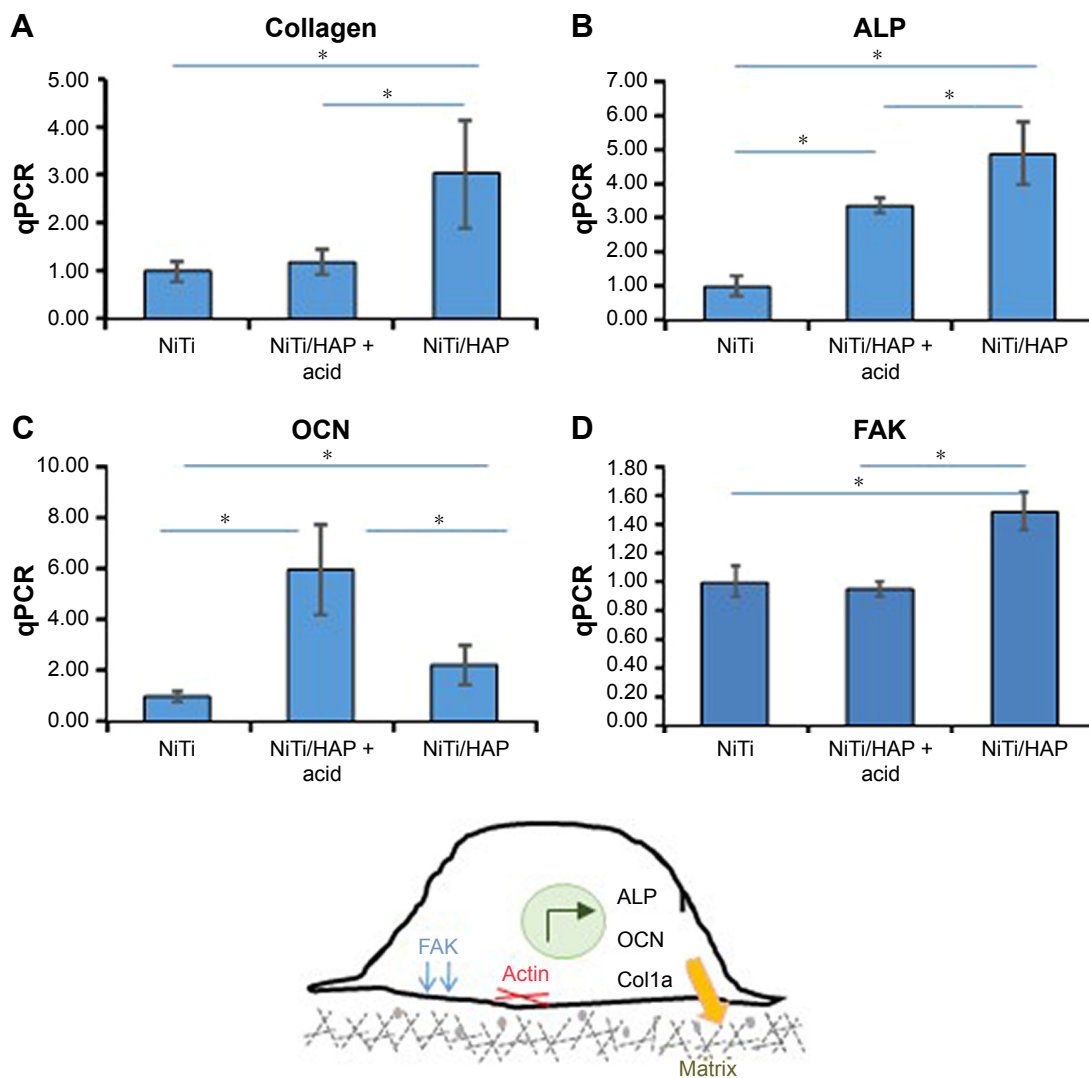


**Figure 5** Expression levels of osteoblast biomarkers on sNiTi, sNiTi/HA-acid, and sNiTi/HA surfaces.

**Notes:** Osteoblasts were differentiated on the three sNiTi surfaces and the mRNA expression of osteoblastic markers was analyzed by qPCR. The relative gene expression was compared for each metal compared with the NiTi control for each gene: (A) collagen type Ia, (B) ALP, (C) OCN, and (D) FAK. qPCR experiments were performed in triplicate and replicated three times, and representatives of these data are shown. GAPDH was used as the housekeeping gene. (\*) indicates statistical significance of  $P < 0.05$ . (E) A schematic representation of an osteoblast is shown. Osteoblasts express ALP, OCN, and collagen type I which are necessary for extracellular matrix formation. Osteoblast adhesion is regulated by actin, FAK, and other focal adhesion proteins (not shown).

**Abbreviations:** ALP, alkaline phosphatase; FAK, focal adhesion kinase; HA, hydroxyapatite; NiTi, nitinol; OCN, osteocalcin; sNiTi, sintered NiTi.

(Figure 5D). As expected, acid etching, which removes the HA coating, resulted in the observed decrease in FAK for the sNiTi/HA-acid plate compared with sNiTi/HA. Other groups have also reported that focal adhesion formation in cells is higher on HA,<sup>53</sup> which is similar in composition to bone apatite and forms 70% by weight of human bone.

To further examine osteoblast activity on the different metals, we performed immunofluorescent microscopy. Osteoblasts were plated on the metals and cultured in osteogenic media. Cells were stained with rhodamine phalloidin (red; Figure 6) which labels filamentous actin (F-actin), a major component of the cellular cytoskeleton.<sup>39</sup> In addition, osteoblasts were stained for collagen type 1 (green).

Nuclei were stained blue with DAPI. Figure 6 shows that osteoblasts on NiTi were uniformly distributed on the metal surface, as indicated by stained nuclei. Of particular interest, the number of cells present on sNiTi/HA was greatly increased compared with the sNiTi/HA-acid or NiTi control, which suggested an increase in the number of cells adhering to and/or proliferating on the sNiTi/HA surfaces. In the NiTi group, both filamentous and punctate F-actin structures which surrounded the central nucleus were observed with phalloidin staining. In addition, collagen expression was largely intracellular. In contrast, when cells were cultured on the HA surfaces, in particular on the sNiTi/HA plate, an increase in F-actin staining was observed, which was largely



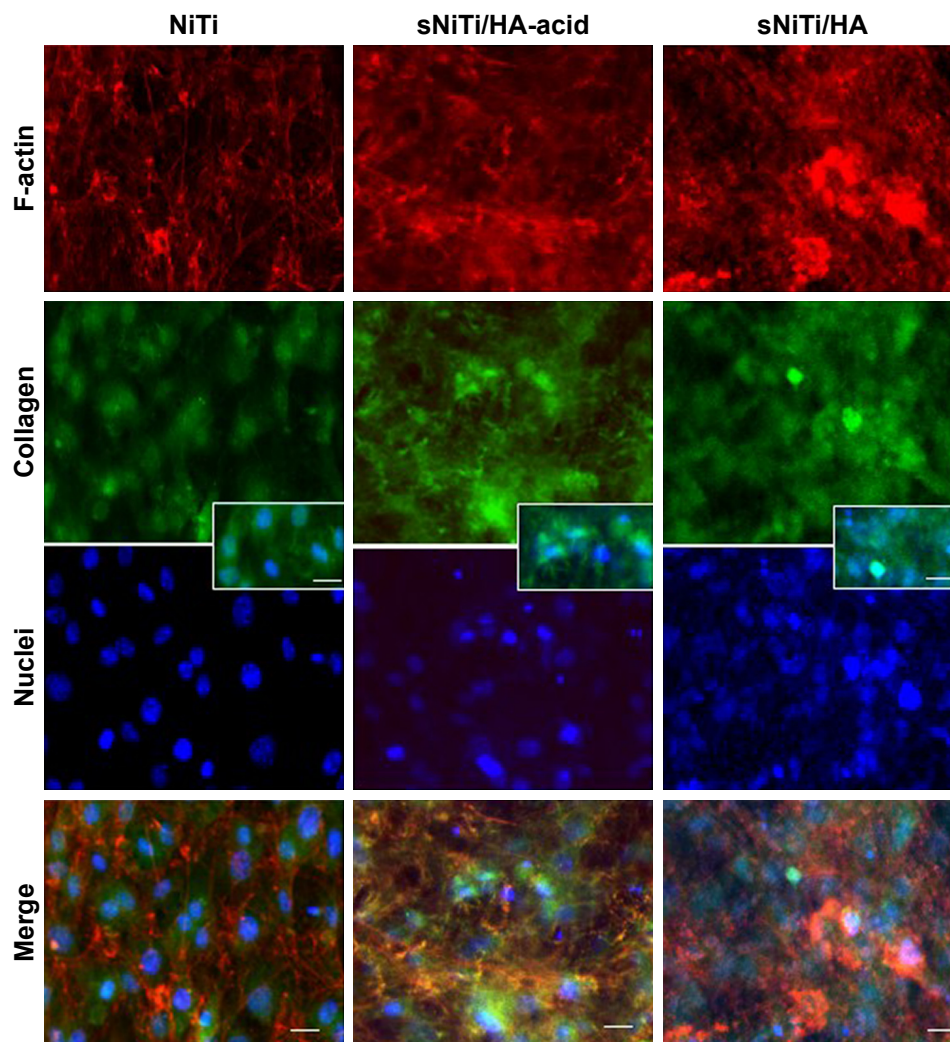


**Figure 6** Immunofluorescent staining of osteoblasts on NiTi, sNiTi/HA-acid, and sNiTi/HA surfaces.

**Notes:** Osteoblasts were differentiated on the metals and then stained for phalloidin which detects filamentous actin (F-actin; red) or collagen (green). Cell nuclei were stained with DAPI (blue). The fluorescent images of each stain are shown separately and as merged image. All images were taken at 20 $\times$ . The scale bar indicates 10  $\mu$ m. The inset shows higher magnification of double-labeled cells showing collagen and cell nuclei for each of the substrates.

**Abbreviations:** HA, hydroxyapatite; NiTi, nitinol; sNiTi, sintered NiTi.

punctate in appearance, indicative of increased cell adhesion. Moreover, the F-actin structures were three-dimensional and disorganized. Finally, as the complexity of the surface structure increased NiTi < sNiTi/HA-acid < sNiTi/HA, we observed an increase in the expression of collagen, with both intracellular and extracellular staining being evident on the sNiTi/HA-acid and sNiTi/HA surfaces, but not on the NiTi plate.

## Conclusion

NiTi implants were additively manufactured by in situ direct laser deposition from Ni and Ti powders. As reported by others, the NiTi implants have similar mechanical property to that of bone. Nanoporous NiTi/HA composite coating was successfully applied on top of the NiTi substrates using an

NPLS process, which utilized a nanosecond laser to sinter the mixture of Ni, Ti, and HA nanoparticles. The surface structure of the composite coating was porous with nanoscale complexity. These complex structures were generated by the pulverization of crystalline HA into nano-HA, which promoted the balling effect of sintering process. Rapid solidification preserves the generated pores before they vanish in the NiTi matrix. This ultrafast heating and cooling process also improved the coating quality by suppressing the generation of undesired phases in the Ni–Ti intermetallic system.

Several of our findings support the effectiveness of using the HA composite coating on sNiTi for osteoblastic bone formation, including the three-dimensional morphology of osteoblasts, the presence of lamellipodial membrane extensions on the HA surfaces, and the increased carbon content



beneath the osteoblast monolayer. Overall, the sNiTi/HA and sNiTi/HA-acid plates also showed higher levels of collagen, ALP, and OCN mRNA expression levels, compared with osteoblasts grown on the control sNiTi plates. In addition, our studies suggest that the HA coating increased osteoblast adhesion, as indicated by an increase in FAK expression, as well as an increase in the number of phalloidin-stained punctate F-actin structures, especially on the sNiTi/HA plates. In addition, we observed increased collagen expression by osteoblasts grown on the sNiTi/HA-acid and sNiTi/HA plates. This finding was consistent with the increase in collagen mRNA expression on sNiTi/HA, as well as increased carbon content on the subcellular surface. Both the HA coating and the porous topology it provided likely contributed to the increased osteoblast activity, cell adhesion, and/or proliferation, as well as increase in collagen expression on the coated sNiTi substrates. Together, our findings demonstrate the capability of using the NPLS method to generate an osteoinductive surface coating on multielement metallic implants. The NPLS method combines the advantages of a biocompatible ceramics-metal composite with the beneficial effects of complex micro-nanosurface structures for bone regeneration applications.

## Acknowledgments

The authors thank National Science Foundation, USA (CMMI Division, Materials Engineering and Processing Program) and National Institute of Standards and Technology, USA for the financial support to GJC. The project was also supported in part by a grant to AB from the National Institute of Health, NIAMS R01-AR060332. We sincerely thank Jung Min Hong, Sumana Posritong for contributions on characterization of the osteoblast activity, and Jeongwoo Lee, and Prof Yung C Shin on characterization of the 3D printed NiTi substrate.

## Disclosure

The authors report no conflicts of interest in this work.

## References

- Chen Q, Thouas GA. Metallic implant biomaterials. *Mater Sci Eng R Rep*. 2015;87:1–57.
- Krishna BV, Bose S, Bandyopadhyay A. Fabrication of porous NiTi shape memory alloy structures using laser engineered net shaping. *J Biomed Mater Res B Appl Biomater*. 2009;89(2):481–490.
- Shabalovskaya SA. Physicochemical and biological aspects of Nitinol as a biomaterial. *Int Mater Rev*. 2001;46(5):233–250.
- Bansiddhi A, Sargeant TD, Stupp SI, Dunand DC. Porous NiTi for bone implants: a review. *Acta Biomater*. 2008;4(4):773–782.
- Singh R, Dahotre NB. Corrosion degradation and prevention by surface modification of biometallic materials. *J Mater Sci Mater Med*. 2007;18(5):725–751.
- Rondelli G, Vicentini B. Localized corrosion behaviour in simulated human body fluids of commercial Ni-Ti orthodontic wires. *Biomaterials*. 1999;20(8):785–792.
- Shabalovskaya S, Anderegg J, van Humbeeck J. Critical overview of Nitinol surfaces and their modifications for medical applications. *Acta Biomater*. 2008;4(3):447–467.
- Liu M, Yue X, Dai Z, Xing L, Ma F, Ren N. Stabilized hemocompatible coating of nitinol devices based on photo-cross-linked alginate/heparin multilayer. *Langmuir*. 2007;23(18):9378–9385.
- Ohgushi H, Okumura M, Yoshikawa T, et al. Bone formation process in porous calcium carbonate and hydroxyapatite. *J Biomed Mater Res*. 1992;26(7):885–895.
- Liu X, Chu P, Ding C. Surface modification of titanium, titanium alloys, and related materials for biomedical applications. *Mater Sci Eng R Rep*. 2004;47(3–4):49–121.
- Ripamonti U, Roden LC, Renton LF. Osteoinductive hydroxyapatite-coated titanium implants. *Biomaterials*. 2012;33(15):3813–3823.
- Roy M, Balla VK, Bandyopadhyay A, Bose S. Compositionally graded hydroxyapatite/tricalcium phosphate coating on Ti by laser and induction plasma. *Acta Biomater*. 2011;7(2):866–873.
- Fathi MH, Salehi M, Saatchi A, Mortazavi V, Moosavi SB. In vitro corrosion behavior of bioceramic, metallic, and bioceramic-metallic coated stainless steel dental implants. *Dent Mater*. 2003;19(3):188–198.
- Cui ZD, Chen MF, Zhang LY, Hu RX, Zhu SL, Yang XJ. Improving the biocompatibility of NiTi alloy by chemical treatments: An in vitro evaluation in 3T3 human fibroblast cell. *Mater Sci Eng C*. 2008;28(7):1117–1122.
- Zhang W, Wang G, Liu Y, et al. The synergistic effect of hierarchical micro/nano-topography and bioactive ions for enhanced osseointegration. *Biomaterials*. 2013;34(13):3184–3195.
- Guo Y, Zhou Y, Jia D, Ha DC. Fabrication of hydroxycarbonate apatite coatings with hierarchically porous structures. *Acta Biomater*. 2008;4(2):334–342.
- Hatakeyama W, Taira M, Chosa N, Kihara H, Ishisaki A, Kondo H. Effects of apatite particle size in two apatite/collagen composites on the osteogenic differentiation profile of osteoblastic cells. *Int J Mol Med*. 2013;32(6):1255–1261.
- Costa DO, Prowse PD, Chrones T, et al. The differential regulation of osteoblast and osteoclast activity by surface topography of hydroxyapatite coatings. *Biomaterials*. 2013;34(30):7215–7226.
- Roy M, Bandyopadhyay A, Bose S. Induction plasma sprayed nano hydroxyapatite coatings on titanium for orthopaedic and dental implants. *Surf Coat Technol*. 2011;205(8–9):2785–2792.
- Nelson M, Balasundaram G, Webster TJ. Increased osteoblast adhesion on nanoparticulate crystalline hydroxyapatite functionalized with KRSR. *Int J Nanomedicine*. 2006;1(3):339–349.
- Dasgupta S, Tarafder S, Bandyopadhyay A, Bose S. Effect of grain size on mechanical, surface and biological properties of microwave sintered hydroxyapatite. *Mater Sci Eng C Mater Biol Appl*. 2013;33(5):2846–2854.
- Tsui YC, Doyle C, Clyne TW. Plasma sprayed hydroxyapatite coatings on titanium substrates. Part I: Mechanical properties and residual stress levels. *Biomaterials*. 1998;19(22):2015–2029.
- Boccaccini AR, Keim S, Ma R, Li Y, Zhitomirsky I. Electrophoretic deposition of biomaterials. *J R Soc Interface*. 2010;7(Suppl 5):S581–S613.
- Dinda GP, Shin J, Mazumder J. Pulsed laser deposition of hydroxyapatite thin films on Ti-6Al-4V: effect of heat treatment on structure and properties. *Acta Biomater*. 2009;5(5):1821–1830.
- Tanahashi M, Yao T, Kokubo T, et al. Apatite Coating on Organic Polymers by a Biomimetic Process. *J Am Ceram Soc*. 1994;77(11):2805–2808.
- Xue W, Tao S, Liu X, Zheng X, Ding C. In vivo evaluation of plasma sprayed hydroxyapatite coatings having different crystallinity. *Biomaterials*. 2004;25(3):415–421.
- Cheang P, Khor KA. Addressing processing problems associated with plasma spraying of hydroxyapatite coatings. *Biomaterials*. 1996;17(5):537–544.

28. Zhang MY, Ye C, Erasquin UJ, Huynh T, Cai C, Cheng GJ. Laser engineered multilayer coating of biphasic calcium phosphate/titanium nanocomposite on metal substrates. *ACS Appl Mater Interfaces*. 2011; 3(2):339–350.
29. Zhang MY, Cheng GJ. Nanoscale size dependence on pulsed laser sintering of hydroxyapatite/titanium particles on metal implants. *J Appl Phys*. 2010;108(11):113112.
30. Zhang MY, Cheng GJ. Pulsed laser coating of hydroxyapatite/titanium nanoparticles on Ti-6Al-4V substrates: multiphysics simulation and experiments. *IEEE Trans Nanobioscience*. 2011;10(3):177–186.
31. Fischer P, Locher M, Romano V, Weber HP, Kolossov S, Glandon R. Temperature measurements during selective laser sintering of titanium powder. *Int J Machine Tools Manufact*. 2004;44(12–13):1293–1296.
32. Zhou J, Tsai HL. Porosity Formation and Prevention in Pulsed Laser Welding. *J Heat Transfer*. 2007;129(8):1014–1024.
33. Schmidt M, Vollertsen F, Geiger M, Shishkovsky I, Yadroitsev I, Smurov I. Laser Assisted Net shape Engineering 7 (LANE 2012) Direct Selective Laser Melting of Nitinol Powder. *Physics Procedia*. 2012;39: 447–454.
34. Otsuka K, Ren X. Physical metallurgy of Ti–Ni-based shape memory alloys. *Prog Mater Sci*. 2005;50(5):511–678.
35. Shishkovskii IV, Yadroitsev IA, Smurov IY. Selective laser sintering/melting of nitinol–hydroxyapatite composite for medical applications. *Powder Metal Met Ceram*. 2011;50(5–6):275–283.
36. Margolis HC, Moreno EC. Kinetics of hydroxyapatite dissolution in acetic, lactic, and phosphoric acid solutions. *Calcif Tissue Int*. 1992;50(2):137–143.
37. Kacena MA, Eleniste PP, Cheng YH, et al. Megakaryocytes regulate expression of Pyk2 isoforms and caspase-mediated cleavage of actin in osteoblasts. *J Biol Chem*. 2012;287(21):17257–17268.
38. Cheng YH, Hooker RA, Nguyen K, et al. Pyk2 regulates megakaryocyte-induced increases in osteoblast number and bone formation. *J Bone Miner Res*. 2013;28(6):1434–1445.
39. Eleniste PP, Patel V, Positong S, et al. Pyk2 and Megakaryocytes Regulate Osteoblast Differentiation and Migration Via Distinct and Overlapping Mechanisms. *J Cell Biochem*. 2016;117(6):1396–1406.
40. Halani PR, Shin YC. In Situ Synthesis and Characterization of Shape Memory Alloy Nitinol by Laser Direct Deposition. *Metal Mater Trans A*. 2012;43(2):650–657.
41. Halani PR, Kaya I, Shin YC, Karaca HE. Phase transformation characteristics and mechanical characterization of nitinol synthesized by laser direct deposition. *Mater Sci Eng A*. 2013;559:836–843.
42. Xu JL, Jin XF, Luo JM, Zhong ZC. Fabrication and properties of porous NiTi alloys by microwave sintering for biomedical applications. *Mater Lett*. 2014;124:110–112.
43. Gu DD, Shen YF. Influence of phosphorus element on direct laser sintering of multicomponent Cu-based metal powder. *Metal Mater Trans B*. 2006;37(6):967–977.
44. Feng P, Niu M, Gao C, Peng S, Shuai C. A novel two-step sintering for nano-hydroxyapatite scaffolds for bone tissue engineering. *Sci Rep*. 2014;4:5599.
45. Khalil-Allafi J, Dlouhy A, Eggeler G. Ni4Ti3-precipitation during aging of NiTi shape memory alloys and its influence on martensitic phase transformations. *Acta Mater*. 2002;50(17):4255–4274.
46. Choi D, Kumta PN. An Alternative Chemical Route for the Synthesis and Thermal Stability of Chemically Enriched Hydroxyapatite. *J Am Ceram Soc*. 2006;89(2):444–449.
47. Bose S, Saha SK. Synthesis of Hydroxyapatite Nanopowders via Sucrose-Templated Sol-Gel Method. *J Am Ceram Soc*. 2003;86(6):1055–1057.
48. Gross KA, Berndt CC, Herman H. Amorphous phase formation in plasma-sprayed hydroxyapatite coatings. *J Biomed Mater Res*. 1998;39(3): 407–414.
49. Golub EE, Harrison G, Taylor AG, Camper S, Shapiro IM. The role of alkaline phosphatase in cartilage mineralization. *Bone Miner*. 1992; 17(2):273–278.
50. Park JW, Kim YJ, Jang JH, Kwon TG, Bae YC, Suh JY. Effects of phosphoric acid treatment of titanium surfaces on surface properties, osteoblast response and removal of torque forces. *Acta Biomater*. 2010; 6(4):1661–1670.
51. Zachary I. Focal adhesion kinase. *Int J Biochem Cell Biol*. 1997;29(7): 929–934.
52. Damsky CH. Extracellular matrix-integrin interactions in osteoblast function and tissue remodeling. *Bone*. 1999;25(1):95–96.
53. Goto T, Yoshinari M, Kobayashi S, Tanaka T. The initial attachment and subsequent behavior of osteoblastic cells and oral epithelial cells on titanium. *Biomed Mater Eng*. 2004;14(4):537–544.

## International Journal of Nanomedicine

### Publish your work in this journal

The International Journal of Nanomedicine is an international, peer-reviewed journal focusing on the application of nanotechnology in diagnostics, therapeutics, and drug delivery systems throughout the biomedical field. This journal is indexed on PubMed Central, MedLine, CAS, SciSearch®, Current Contents®/Clinical Medicine,

Submit your manuscript here: <http://www.dovepress.com/international-journal-of-nanomedicine-journal>

Dovepress

Journal Citation Reports/Science Edition, EMBASE, Scopus and the Elsevier Bibliographic databases. The manuscript management system is completely online and includes a very quick and fair peer-review system, which is all easy to use. Visit <http://www.dovepress.com/testimonials.php> to read real quotes from published authors.